Available online at www.sciencedirect.com
ScienceDirect
Geochimica et Cosmochimica Acta 71 (2007) 3257–3271
Geochimica et Cosmochimica Acta
www.elsevier.com/locate/gca

Aqueous Cr(VI) reduction by pyrite: Speciation and characterisation of the solid phases by X-ray photoelectron, Raman and X-ray absorption spectroscopies

Martine Mullet [a,*], Frédéric Demoisson [a], Bernard Humbert [a], Laurent J. Michot [b], Delphine Vantelon [c]

[a] *Laboratoire de Chimie Physique et Microbiologie pour l'Environnement (LCPME), UMR 7564 CNRS-Université Henri Poincaré-Nancy 1, 405, rue de Vandœuvre, F-54600 Villers-lès-Nancy, France*

[b] *LEM, Laboratoire Environnement et Minéralurgie, UMR 7569 CNRS and INPL, Ecole Nationale Supérieure de Géologie, BP 40, 54501 Vandoeuvre-lès-Nancy, France*

[c] *SOLEIL, BP 48, F-91192 GIF/Yvette, France*

Received 2 May 2006; accepted in revised form 6 September 2006; available online 12 October 2006

Abstract

Optical microscopy, confocal Raman micro-spectrometry, X-ray photoelectron micro-spectroscopy (XPS) and synchrotron based micro-X-ray fluorescence (XRF), micro-X-ray absorption near edge spectroscopy (XANES) and micro-extended X-ray absorption fine structure (EXAFS) were used to investigate the reduction of aqueous Cr(VI) by pyrite. Special emphasis was placed on the characterisation of the solid phase formed during the reaction process. Cr(III) and Fe(III) species were identified by XPS analyses in addition to non-oxidised pyrite. Optical microscopy images and the corresponding Raman spectra reveal a strong heterogeneity of the samples with three different types of zones. (i) Reflective areas with E_g and A_g Raman wavenumbers relative to non-oxidised pyrite are the most frequently observed. (ii) Orange areas that display a drift of the E_g and A_g pyrite vibration modes of -3 and $-6\ cm^{-1}$, respectively. Such areas are only observed in the presence of Cr(VI) but are not specifically due to this oxidant. (iii) Bluish areas with vibration modes relative to a corundum-like structure that can be assigned to a solid solution $Fe_{2-x}Cr_xO_3$, x varying between 0.2 and 1.5. The heterogeneity in the spatial distribution of chromium observed by optical microscopy and associated Raman microspectroscopy is confirmed by μ-XRF. In agreement with both solution and XPS analyses, these spectroscopies clearly confirm that chromium is in the trivalent state. XANES spectra in the iron K-edge pre-edge region obtained in rich chromium areas reveal the presence of ferric ion thus revealing a systematic association between Cr(III) and Fe(III). In agreement with Raman analyses, Cr K-edge EXAFS can be interpreted as corresponding to Cr atoms involved in a substituted-type hematite structure $Fe_{2-x}Cr_xO_3$.

1. INTRODUCTION

Pyrite (FeS_2) is the most abundant phase in sulfide ore deposits (Vaughan and Lennie, 1991). Its weathering is the main process leading to acid mine drainage. Pyrite weathering implies a combination of oxidation and dissolution processes and usually involves ferric iron and oxygen, the two most important oxidants in natural waters (Lowson, 1982; McKibben and Barnes, 1986; Moses Carl et al., 1987). It is also very sensitive to microbial activity that significantly increases pyrite leaching (Hansford and Vargas, 2001; Brett and Banfield, 2003; Rodriguez et al., 2003). Furthermore, pyrite is also distributed as a minor phase in a variety of geological settings and notably, is an ubiquitous component in reduced environments where it acts as a reservoir of reductants for hazardous oxidised species, such as chlorinated organic molecules (Davis et al., 2003) and metal anions (Francis et al., 1989; Zouboulis et al., 1993; Doyle et al., 2004).

* Corresponding author.
E-mail address: mullet@lcpme.cnrs-nancy.fr (M. Mullet).

0016-7037/$ - see front matter © 2006 Elsevier Ltd. All rights reserved.
doi:10.1016/j.gca.2006.09.008

However, despite its environmental importance, the detailed oxidation pathway of pyrite minerals remains partially unknown. In that context, the present study is concerned with the reduction of Cr(VI) by pyrite. Various industrial applications (tannery, metallurgy, electroplating…) generate effluents with significant Cr(VI) content and poor storage conditions of the wastes can lead to the release of Cr(VI) in the environment. Cr(VI) is well known to be highly toxic and soluble, whereas its reduced form Cr(III) is much less toxic and less soluble (Norseth, 1981; Myers et al., 2000). In particular, Cr(III) is expected to strongly sorb at mineral surfaces where it may form hydroxide solids of low solubility, thus reducing its transport in groundwater or in natural settings. In that regard, pyrite could play an important role by controlling the redox species of chromium. It is therefore of critical importance to understand in depth the mechanisms leading to Cr(VI) reduction by pyrite and the subsequent sorption of Cr(III) compounds.

Much work has been devoted to Cr(VI) reduction by ferrous ions in solution (Eary and Rai, 1988; Fendorf and Li, 1996; Buerge and Hug, 1997; Pettine et al., 1998; Schlautman and Han, 2001), iron bearing materials such as oxides (Eary and Rai, 1989; Peterson et al., 1997a; Kendelewicz et al., 2000) and more recently green rusts (Loyaux-Lawniczak et al., 2000; Williams and Scherer, 2001). In comparison, fewer studies have been carried out on aqueous Cr(VI) reduction by pyrite (Zouboulis et al., 1995; Kim et al., 2002; Doyle et al., 2004) and other sulfide minerals (Patterson et al., 1997; Mullet et al., 2004). Most of these works have focused mainly on the efficiency of iron sulfides for removing Cr(VI) from solution and have thus been devoted to the characterisation of solutions and solid phase products under different applied experimental conditions. Our previous study investigated the aqueous processes leading to Cr(VI) reduction by pyrite under argon atmosphere (Demoisson et al., 2005). In the pH range from 2 to 8, the time evolution of metal species concentrations exhibited two distinct trends depending on the amount of Cr(VI) removed from solution. Detailed analyses of the chemical pathways in solution revealed that both iron and sulphur species are oxidised to generate aqueous Cr(III) and Fe(III), the appearance of Fe(II) in solution being only observed in experiments where a total removal of Cr(VI) was achieved. The mass balance on chromium species suggested the existence of sorbed or precipitated chromium species in the solid phase, the nature of which remains ill defined. The goal of the present paper is then to characterise in detail the nature of the solid phases resulting from the previously described reaction by a combination of optical microscopy, confocal Raman micro-spectrometry, X-ray photoelectron micro-spectroscopy and synchrotron based micro-X-ray fluorescence, micro-X-ray absorption near edge spectroscopy and micro-extended X-ray absorption fine structure.

2. EXPERIMENTAL

2.1. Materials

The iron sulfide used in this study was a synthetic pyrite (FeS_2, 99.9% pure) purchased from Alpha Aesar. The mineral was characterized using transmission electron microscopy (TEM) combined with electron diffraction and energy dispersive spectrometry (EDS). The crystal structure (*Pa3*) confirms the single pyritic phase with a S/Fe ratio of 2.0 ± 0.1. The surface area of the sample measured by nitrogen adsorption at 77 K and determined by BET treatment is $0.7 \pm 0.2\ m^2\ g^{-1}$. In order to obtain a clean surface, the pyrite was washed in deoxygenated deionised water (Milli-Q, 18.2 $M\Omega\ cm^{-1}$ resistivity) for 2 h and then placed inside a glovebox (Jacomex TM controlled atmosphere glovebox) where it was first dried in the vacuum chamber (10^{-2} Torr) before being stored under argon atmosphere until use. The absence of oxide contaminants was checked by X-ray photoelectron and Raman spectroscopy. Optical microscopy images (not shown) reveal homogeneous pyrite particles with their typical shiny aspect and a Raman spectrum (Fig. 1) only displays signals at 340 and 377 cm^{-1} that can be assigned to E_g and A_g vibration modes of pyrite, respectively (Sourisseau et al., 1991).

2.2. Batch experiments

Experiments were conducted under an argon atmosphere using a Teflon® reactor to reduce adsorption of reactants to the reactor surfaces. The reactor was HNO_3 cleaned and rinsed with ion-exchanged water between experiments to avoid possible contamination. All reactions were carried out in a 0.1 M $NaClO_4$ supporting electrolyte that was pre-equilibrated under a flowing argon atmosphere for 2 h. Weighed amounts of pretreated pyrite were then added to the reactor to reach a 6 $g\ L^{-1}$ concentration, and equilibrated in the inert electrolyte for approximately 90 min under vigorous stirring. An appropriate stock solution of potassium chromate K_2CrO_4 (Analytical grade VWR®) was then added to the pyrite suspension to give initial Cr(VI) concentrations in the range $1–7 \times 10^{-4}$ M while the pH was adjusted in the range of 2–8 by $HClO_4$. pH was constantly monitored and adjusted for 20 h using a computer-controlled titrator and a Ross pH electrode. Samples were withdrawn from the system at different time intervals for chromium and iron analyses by UV–Vis spectroscopy (Demoisson et al., 2005). After the 20 h period, the samples were filtered through 0.22 μm membrane filters. The resulting solids were freeze-dried and stored in the vacuum chamber of the glove box until analysis.

2.3. Characterization methods

2.3.1. X-ray photoelectron spectroscopy

XPS spectra were obtained using a KRATOS Axis Ultra X-ray photoelectron spectrometer with a monochromatized Al Kα X-ray source ($h\nu = 1486.6$ eV) operated at 150 W. The samples were pressed onto a Cu tape on a holder and introduced into the spectrometer. The base pressure in the analytical chamber was $\approx 10^{-9}$ mbar. Spectra were collected at normal (90°) take-off angle. Survey scans were used to determine the chemical elements at the pyrite surface. They were acquired with a pass energy of 160 eV and a X-ray spot size of 0.3 mm × 0.7 mm. Narrow region photoelectron spectra were used to determine chemical state information. They were acquired with an analyser pass energy of 20 eV

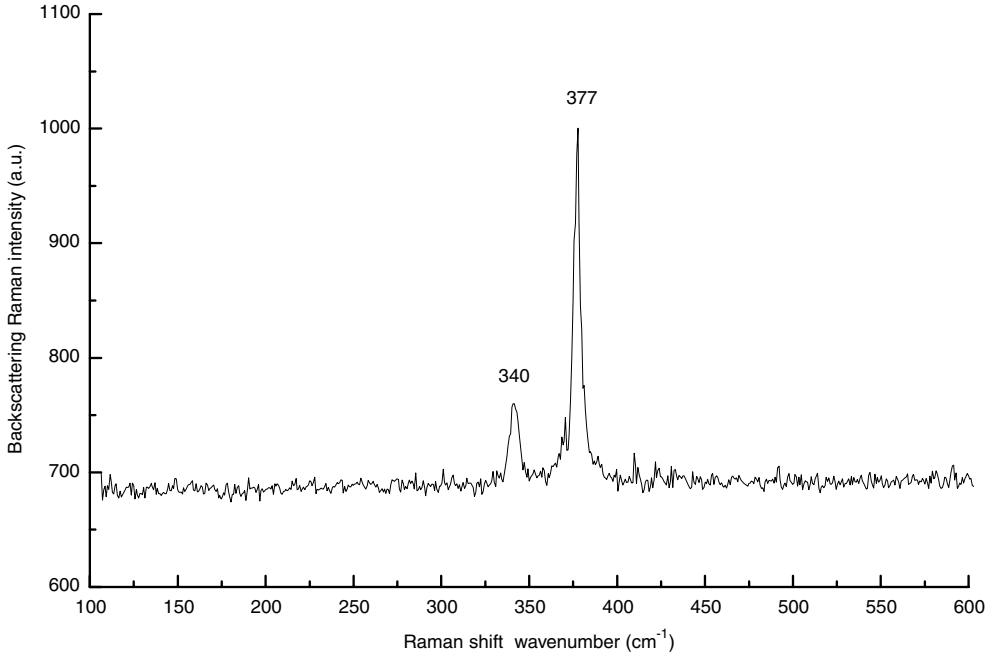

Fig. 1. Raman spectrum of a shiny portion of a washed pyrite surface. The only scattering signals are pure pyrite phonons E_g and A_g at 340 and 377 cm^{-1}, respectively.

and an X-ray spot size of 0.3 mm × 0.7 mm. The binding energy was calibrated by assigning the C(1 s) peak to 284.6 eV. Spectra for iron, sulphur, and chromium were fitted using a Shirley Background (Shirley, 1972) and a pseudo-voigt peak model.

2.3.2. Raman spectroscopy

Raman spectra were recorded with a triple substractive monochromator T64000 Jobin Yvon spectrometer equipped with a confocal microscope. The detector was a charged coupled device (CCD) cooled by liquid nitrogen. The samples were excited by a laser beam at 514 nm and 488 nm emitted by an Argon Laser (Stabilite 2017, Spectra Physics) with a power of about 2 mW and focused with a diameter of about 0.8 μm on the sample. The Raman backscattering was collected through the microscope lens (×100) and dispersed by a 1800 grooves/mm grating to obtain 2.7 and 2.9 cm^{-1} spectral resolutions for the 514 and 488 nm excitation beams, respectively. The wavenumber accuracy in vacuum was better than 0.8 cm^{-1}. The polarization discrimination of the optical device was checked by measuring the depolarization ratios for known bands of reference liquid products. For instance, the experimental depolarization ratio for the 459 cm^{-1} symmetric component of the CCl_4 spectrum is 0.020 ± 0.005 cm^{-1} or 0.03 ± 0.01 cm^{-1} for the C–H stretching mode of CH_2Cl_2. The confocal Raman microprobe is built around an Olympus microscope equipped with a motorized *XY* stage with a step of 80 nm. The lateral resolution value is determined from the displacement necessary to pass from the maximum collected signal to the minimum one the boundaries of gold lines on a calibrated silicon grid. Using such a system, a lateral resolution value of 700 nm was obtained for both excitation wavelengths, whereas the theoretical values based on optical diffraction applied to a perfect Gaussian laser beam and a perfect optical device are 270 and 250 nm (Barbillat et al., 1994) for the lateral resolution and 800 and 700 nm for the axial resolution in non-absorbing materials. With pyrite, which strongly absorbs visible light, this last value is meaningless since the laser penetration in the material decreases exponentially with depth. By computation using the complex refractive index values and an optical check a rough value of less than 100 nm can be estimated for the analyzed depth.

2.3.3. X-ray absorption spectroscopy

X-ray absorption experiments were carried out on beamline LUCIA at the Swiss Light Source PSI, Villigen (2.4 GeV, 350 mA). The overall setup is described by Flank et al. (2006). The X-rays were monochromatized using a Si(1 1 1) double crystal and focused to a beam size of 4 × 6 μm using a Kirpatrick–Baez device (Kirkpatrick and Baez, 1948). Micro-X-ray fluorescence experiments were carried out using steps of 3 μm and counting times of 1 s with incident energies of 6025 or 5997 eV. The fluorescence signal was detected using a solid state silicon drift diode detector. X-ray absorption near edge structure (XANES) spectra were recorded in fluorescence mode at room temperature around the Fe–K edge (7111 eV) with 0.3 eV steps and 1 s collecting time between 7090 and 7200 eV and around the Cr–K edge with 0.3 eV steps and 1 s collecting time between 5975 and 6070 eV. Extended X-ray Absorption Fine Structure (EXAFS) spectra were recorded around the Cr–K edge in fluorescence mode at room temperature with 2 eV steps and 1 s collecting time between 5900 and 6900 eV.

EXAFS data were reduced using software written by Michalowicz (Michalowicz, 1990). A Kaiser window was used for deriving Fourier transform from $k^3 \cdot \chi(k)$ EXAFS spectra. The radial distributions functions (RDF) thus obtained are not corrected for phase shift, which leads to peaks shifted down by ~0.3 Å compared with crystallographic distances. Theoretical phase shifts and amplitude backscattering functions were calculated from the structural model of eskolaite (Cr_2O_3) and bracewellite (CrOOH) using FEFF7.0.2 code (Zabinsky et al., 1995). Numbers and distances of nearest neighbours were derived from least-square fitting, first on individual contributions and finally refined on complete spectra. The accuracy on distances, Debye–Waller factors and number of neighbours can be estimated at ± 0.01Å, ± 10% and ± 20%, respectively (Teo, 1986).

3. RESULTS AND DISCUSSION

3.1. Aqueous metal species concentrations versus time

Typical changes in iron and chromium concentrations with time at pH values of 2 and 5 and an initial Cr(VI) concentration of approximately 1.9×10^{-4} M are shown in Fig. 2. As a previous study was entirely devoted to the investigation of aqueous chemical processes occurring upon pyrite oxidation by Cr(VI) (Demoisson et al., 2005), only the main results are recalled in the present paper. Fig. 2 reveals that the amount of Cr(VI) removed from solution depends on the pH value. For instance, less than 240 min are sufficient for complete Cr(VI) removal at pH 2 (Fig. 2A), whereas incomplete Cr(VI) removal is observed at the time scale of the experiment (around 1200 min) at pH 5 (Fig. 2B). In response to Cr(VI) disappearance with time, Cr(III) concentration increases until reaching plateau when complete Cr(VI) removal is achieved at the time scale of the experiment. At pH 2, the disappearance of Cr(VI) is linked to the appearance of ferric ion, whose concentration increases with decreasing Cr(VI) concentration. Once all Cr(VI) has disappeared, ferric ion concentration decreases while ferrous concentration increases. After complete Cr(VI) removal, pyrite is then oxidized by ferric ion to generate ferrous ions (Demoisson et al., 2005). Ferric ion is not observed in experiments carried out at pH 5 (Fig. 2B) because at such pH the solubility product of ferric iron oxyhydroxides is exceeded (Baes and Mesmer, 1976).

3.2. Surface analysis by XPS

Fe($2p_{3/2}$) and Cr(2p) narrow scans of pyrite samples reacted at pH 2 and pH 5 with ~1.9×10^{-4} M Cr(VI) solution are shown in Fig. 3. At both pHs, the Fe($2p_{3/2}$) spectra exhibit contributions from different iron surface species (Figs. 3A and C). The main contribution at 707.2 eV corresponds to sulphur-bonded Fe(II) in pyrite (Schaufuß et al., 1998). As it is in the low spin state, it occurs as a narrow single peak. The high energy tail of the spectrum is fitted with components at 709, 711.2 and 713 eV, most of them being composed of several multiplet lines. Note that only the broad envelop containing the multiplet peaks is displayed in Fig. 3. The peak located at 713 eV is a broad Fe(II) satellite (shake-up) approximately 5.8 eV above the main peak. The peak arising at 709 eV can be assigned to Fe(II)–O and/or Fe(III)–S species. The Fe($2p_{3/2}$) component for Fe(II)–O is located near 708.5–709.5 eV (McIntyre and Zetaruk, 1977) while multiplet peaks occur in the energy range 709.1–711.4 eV for Fe(III)–S (Schaufuß et al., 1998). Due to the similarity in binding energy range for Fe(II)–O and Fe(III)–S bonds it is truly difficult to clearly distinguish between those two possible assignments. According to Nesbitt et al. (1998), the presence of Fe(III)–S species could result from the breaking of Fe–S bonds at the surface, an electron being transferred from iron to sulphur thus leading to the formation of Fe^{3+} surface sites. Another proposed mechanism relates the presence of a Fe(II)–O component to surface hydroxylation processes (Eggleston et al., 1996). Finally, the peak located at 711.2 eV corresponds unambiguously to oxygen-bonded ferric ion (Fe(III)–O). The presence of this last component agrees with both solution analyses (Fig. 2B and Demoisson et al., 2005) that reveal the disappearance of ferric species in slightly acidic solutions and Raman analyses that evidence the formation of a ferric oxide phase. This last point will be discussed in Section 3.3.

Narrow scans of Cr($2p_{3/2}$) regions were collected to evaluate the oxidation state of chromium species at the pyrite surface (Figs. 3B and D). Unfortunately, the low intensity of Cr(2p) signals does not allow for unambiguous fitting of the spectra. Chromium species occur mainly in solution at pH 2, as revealed by the marginal difference between initial Cr(VI) and final Cr(III) concentrations in Fig. 2A: only around 3.83×10^{-6} mol g^{-1} of the initial Cr(VI) concentration is removed from the solution (Demoisson et al., 2005). The amount of chromium removed from solution is higher at pH 5 (8.33×10^{-6} mol g^{-1}, Fig. 2B) and accordingly the Cr(2p) signal is clearly evidenced (Fig. 3D). The Cr(2p) signal increases from 0.8% to 8% when pH increases from 2 to 5. It should be noted that the magnitude of the spin–orbit splitting between $2p_{1/2}$ and $2p_{3/2}$ peaks depends on the oxidation state of chromium (Allen et al., 1974; Ikemoto et al., 1976). Allen et al. (1974) observed a spin orbit splitting of 9.7–9.9 eV in Cr(III) compounds and 8.7–9.4 eV in Cr(VI) compounds. Furthermore, the binding energy range of the $2p_{3/2}$ peak is 576.4–577.0 eV in Cr(III) compounds, while it is 578.3–579.8 eV in Cr(VI) compounds. In the present study the $2p_{3/2}$ line is centred at 577.1 eV and the spin orbit splitting is 9.9 eV which is characteristic of Cr(III). Doyle et al. (2004) have accordingly evidenced the reduction of Cr(VI) to Cr(III) at fractured pyrite surfaces reacted with Cr(VI) solutions.

3.3. Optical microscopy and micro-Raman spectroscopy

Raman experiments focus on experiments carried at high initial Cr(VI) concentration, for which it should be easier to observe chromium species at the pyrite surface. Fig. 4 displays the optical microscopy images and Raman spectra collected on some selected areas of the sample obtained at pH 2 for an initial Cr(VI) concentration of 6.60×10^{-4} M, whereas Figs. 5 and 6 correspond to exper-

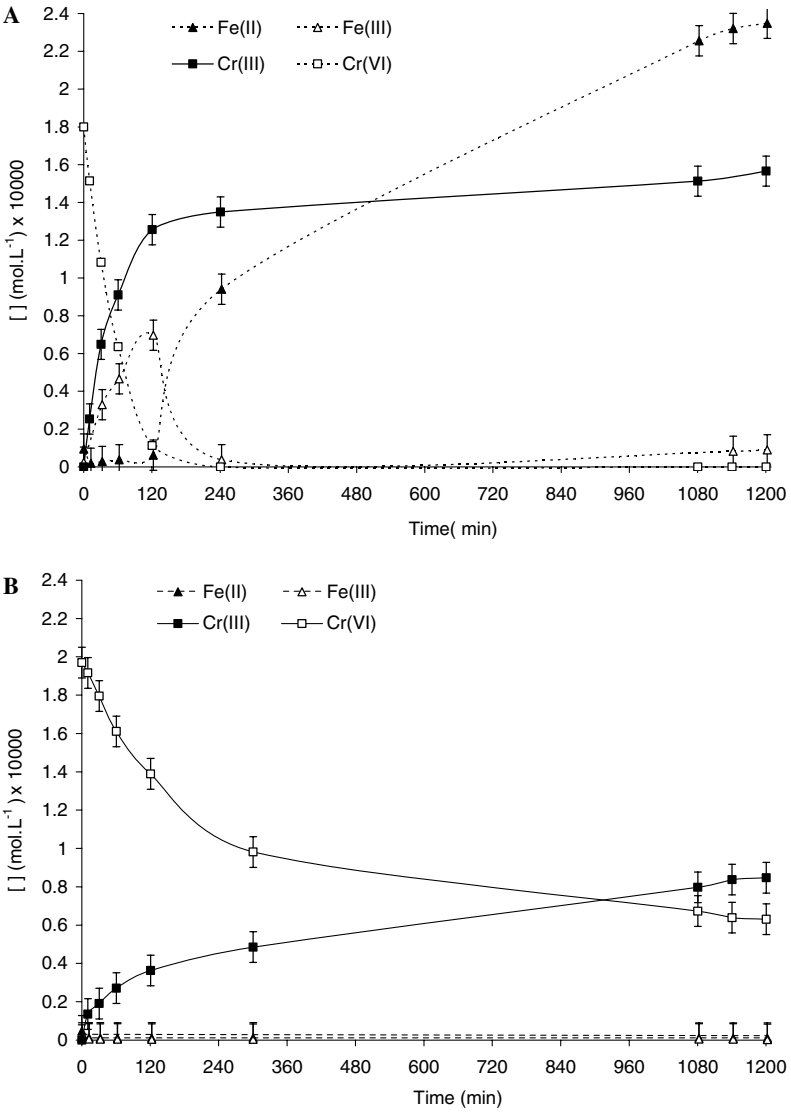

Fig. 2. Changes in iron and chromium concentration with time for pyrite oxidation experiments with an initial Cr(VI) concentration of (A) 1.80×10^{-4} M, pH 2 and (B) 1.97×10^{-4} M, pH 5.

iments carried out at pH 5 for initial Cr(VI) concentrations of 1.97×10^{-4} M and 4.95×10^{-4} M, respectively.

Optical microscopy images of sample reacted at pH 2 reveal a strong heterogeneity with zones with various colours (Figs. 4A–C). The analysis of Raman spectra corresponding to these different zones confirms the structural origin of such changes in colours.

(i) "Reflective" areas (Fig. 4A) are characterized by shift Raman wavenumbers of 340, 377 and 428 cm^{-1} that are assigned to E_g, A_g and T_{g3} vibration modes of non-oxidised pyrite, respectively, (Vogt et al., 1983).

(ii) Some "orange" areas (Fig. 4B) display that the E_g and A_g pyrite vibration modes drift of −3 and −6 cm^{-1}, respectively, in comparison with pyrite. Such observations are not specifically due to oxidation by Cr(VI). Indeed similar band evolutions were also observed in the presence of dissolved oxygen as the only pyrite oxidant in the system (data not shown).

(iii) Some "bluish" areas (Fig. 4C) are characterized by strong signals around 220, 285 and 600 cm^{-1}. These bands are usually assigned to the vibration modes of a corundum-like structure. The wavenumbers are consistent with hematite phase (α-Fe_2O_3) that belongs to the crystal space group D^6_{3d} (Hart et al., 1975; Martin et al., 1977; McCarty and Boehme, 1989; Massey et al., 1990; Shim and Duffy, 2001). Seven phonon lines are expected in the fundamental first order Raman, corresponding to two A_{1g} and five E_g modes. The A_{1g} modes are given in the literature at 224–227 and 494–498 cm^{-1}, while the E_g modes are at 244–248, 290–294, 298–300 and 609–614 cm^{-1}. The Raman spectrum of the bluish areas

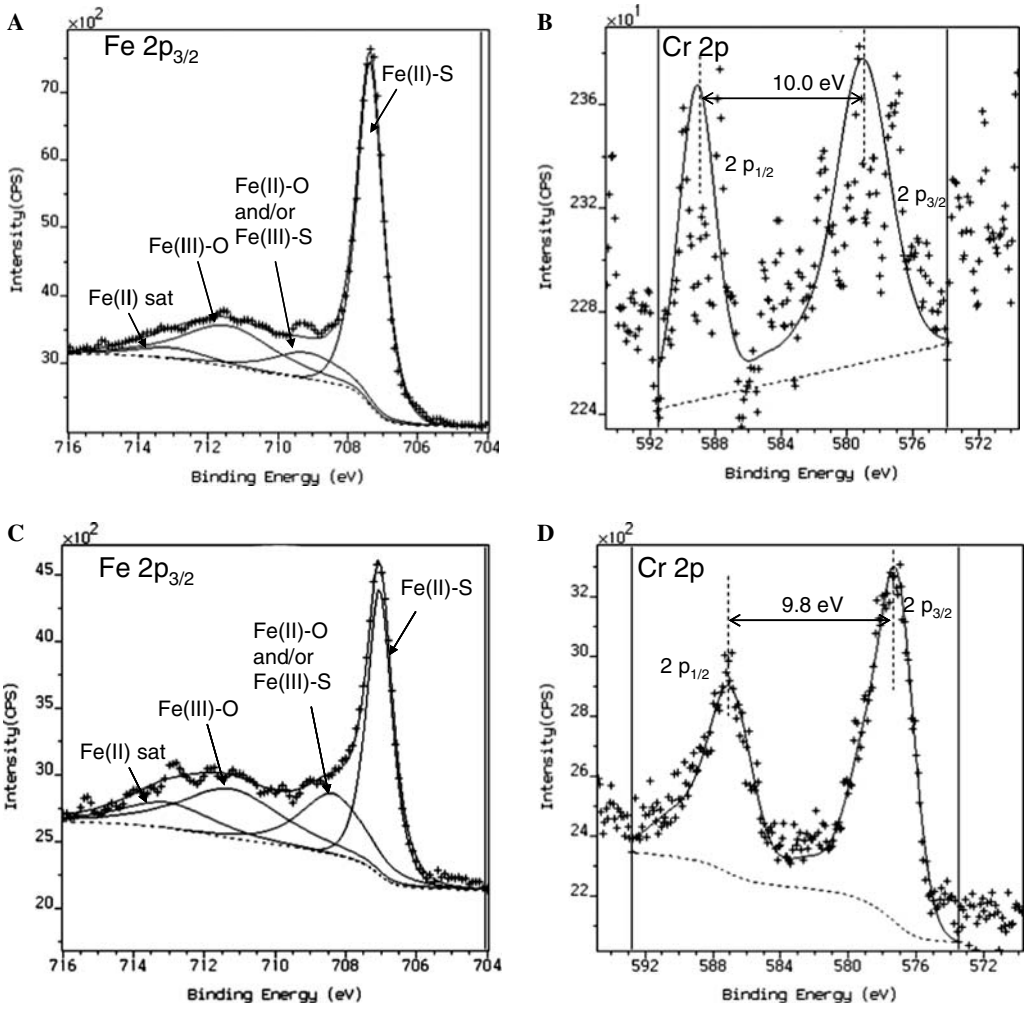

Fig. 3. Fitted Fe($2p_{3/2}$) (A) and Cr(2p) (B) XPS spectra of pyrite for experiment carried out at pH 2 and an initial 1.80×10^{-4} M Cr(VI) solution. Fitted Fe($2p_{3/2}$) (C) and Cr(2p) (D) XPS spectra of pyrite for experiments carried out at pH 5 and a 1.97×10^{-4} M Cr(VI) solution. For Cr(2p) level, the low intensity of the signal did not allow to fit the spectra and the solid line is only drawn as a visual help.

of our pyrite sample displays the two A_{1g} modes exactly at 220 and 495 cm^{-1}. These wavenumbers are lower than those expected for pure hematite and may be explained either by a heating effect due to the focused laser beam or by a structural difference with the usual hematite mineral. Indeed, De Faria et al. (1997) have demonstrated that the laser power focused on a small area of hematite is able to produce a drift of the A_{1g} modes from 227 to 219 and from 498 to 492 cm^{-1}. This hypothesis could be confirmed by the large full width at half height of 12 and 20 cm^{-1}, respectively. However, this heating hypothesis explains neither the blue colour of these areas nor the observed profile around 600 cm^{-1}. Furthermore, an additional broad and strong component around 656 cm^{-1} is also observed. This wavenumber position is not compatible with spinel phases characterized by A_{1g} mode wavenumbers higher than 670 cm^{-1} (from 668 cm^{-1} for magnetite phase (Fe_3O_4) to 690 cm^{-1} for $FeCr_2O_4$). The observed wavenumber at 656 cm^{-1} should then rather be assigned to $Fe_{2-x}Cr_xO_3$ solid solutions. Indeed, McCarty and Boehme (1989) have shown that upon chromium substitution in hematite, a new band appears and shifts from 660 to 685 cm^{-1} when x increases from 0.2 to 1.5. This shift increases nearly linearly with increasing chromium content. For an x value of 2, i.e., pure Cr_2O_3, this band disappears and the total Raman profile is clearly different with an intense band at 530 cm^{-1} that dominates the whole spectrum. It then appears very reasonable to interpret the recorded Raman spectra of the blue areas as corresponding to $Fe_{2-x}Cr_xO_3$ solid solutions. The Raman band at 656 cm^{-1} could then be assigned to the infrared active (and Raman inactive) normal mode in the $R\bar{3}c$ crystal structure, that becomes Raman active in the mixed metal solid solutions as a result of symmetry relaxation. According to McCarty and Boehme (1989), the center of this broad component at 656 cm^{-1} would indicate a value of x smaller than 0.2 in the formula $Fe_{2-x}Cr_xO_3$. However, the signals observed in our samples are much wider than the

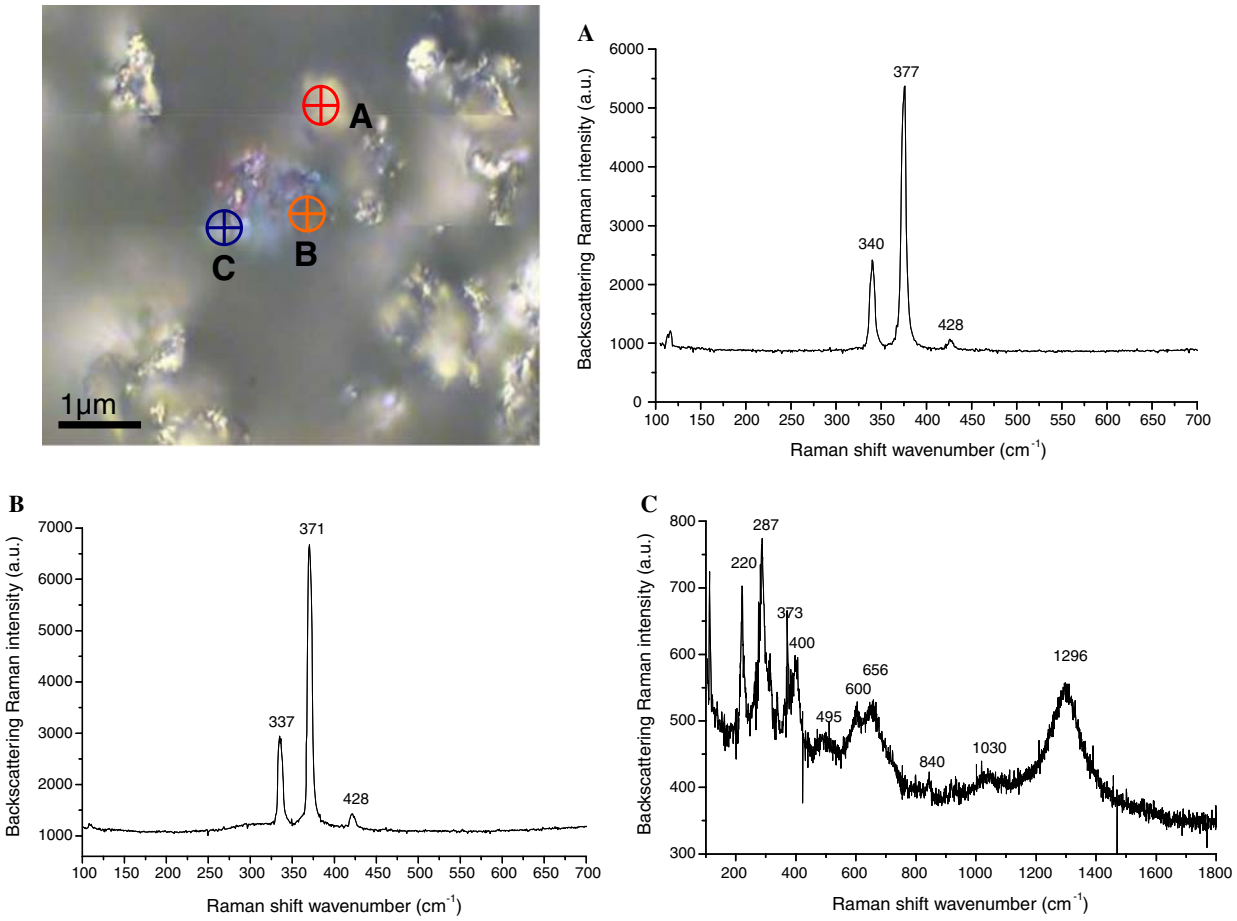

Fig. 4. Optical microscopy image and Raman spectra collected on some representative (A) shining particles of pyrite, (B) orange areas and (C) bluish areas. The experiment was carried out at pH 2 and 6.60×10^{-4} M Cr(VI) initial concentration. (For interpretation of the references to colour in this figure legend, the reader is referred to the web version of this paper.)

ones obtained by these authors, which suggests a distribution of x values in the probed area; a shoulder around 685 cm^{-1} can also be observed in some cases (Fig. 4C). This interpretation is confirmed by the wide profile recorded around 1300 cm^{-1} (band assigned to overtones of fundamental vibrational modes displayed for mixed metal solutions, McCarty and Boehme, 1989). In summary, the observed Raman spectra are very likely due to the presence of $Fe_{2-x}Cr_xO_3$ solid solutions, in which the values of x range between 0.2 and 1.5. In view of the signal to noise ratio and possible heating effects under the laser beam, it is difficult to provide more accurate compositions. In addition, mixtures of nanograins of variable compositions might be present in the micrometer-scale probed area. The presence of relatively intense signals at 337 and 371 cm^{-1} that can be assigned to the underlying oxidized pyrite confirms the very small thickness of the oxide phases formed at the pyrite surface in bluish areas.

At pH 5 and for an initial Cr(VI) concentration of 1.97×10^{-4} M, mainly orange (Figs. 5A and B) and shining zones (Fig. 5C) are observed with Raman spectra similar to those described at pH 2. In contrast, very few bluish areas were observed, which may be linked to the low chromium concentration removed from solution (8.33×10^{-6} mol g^{-1}). This assumption was confirmed by data collected at pH 5 for a high initial Cr(VI) concentration (4.95×10^{-4} M) (Fig. 6) where numerous blue areas (Fig. 6A) relative to the corundum-like structure were observed in addition to orange (Fig. 6B) and shining areas (Fig. 6C). In this latter case, the thickness of the deposited hematite is higher than at pH 2 as the vibration modes of the underlying pyrite are not observed.

3.4. Spatial distribution and analysis of the oxidation state of chromium species by μ-XRF

In view of the small amount of chromium observed in both XPS and Raman analyses of pyrite sample reacted at pH 2, μ-XRF experiments focused on experiments carried out at pH 5. Typical chromium maps are presented in Fig. 7. Map A is obtained an initial Cr(VI) concentration of 1.97×10^{-4} M, whereas maps B to D correspond to samples reacted with an initial Cr(VI) concentration of 4.95×10^{-4} M. Maps B and D correspond to the exact same area analyzed by using two different energies of the

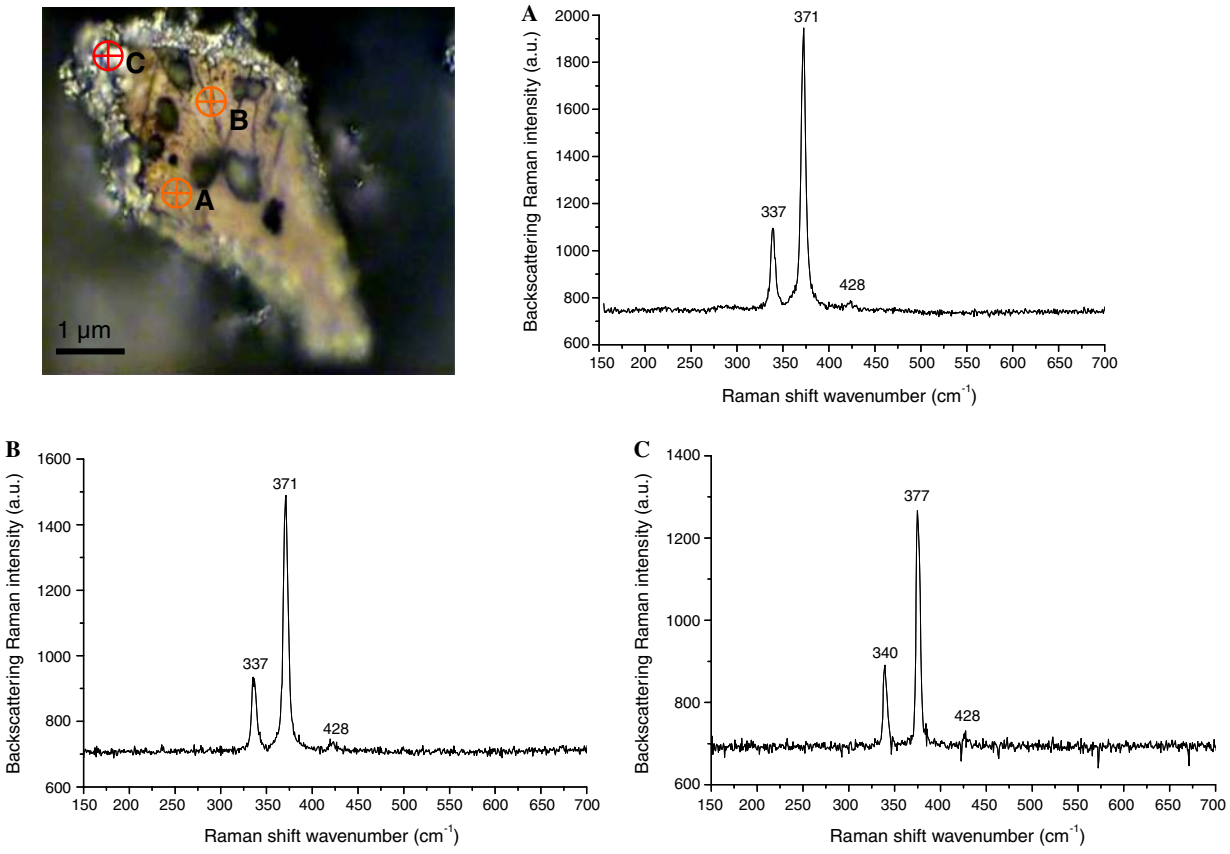

Fig. 5. Optical microscopy image and Raman spectra collected on some representative (A) and (B) orange areas and (C) shining particles of pyrite areas. The experiment was carried out at pH 5 and 1.97×10^{-4} M Cr(VI) initial concentration.

incident X-ray beam at 6025 and 5997 eV, respectively. Whatever the incident energy and initial Cr(VI) concentration, the spatial distribution of chromium is very heterogeneous with a few small size "hot spots" unevenly dispersed, which confirms optical microscopy and Raman microspectroscopy results. Compared with map C that corresponds to a single large pyrite grain, this heterogeneity appears more marked in maps A and B which correspond to numerous small pyrite grains. The influence of the initial chromium concentration is evidenced by the average intensity of map A which is 2.5 times lower than that of map B. Furthermore, for low initial Cr concentration, areas corresponding to high chromium content appear smaller. Such an observation agrees with optical microscopy and associated Raman analyses in which blue areas relative to the presence of chromium were rarely observed.

In terms of chromium oxidation state, various points must be considered. (i) When working with high brilliance focused XAS beamlines, evolution of Cr redox state can be suspected. Such phenomena were indeed observed for Cr contaminated soils (Tokunaga et al., 2003). In the present case, the existence of such radiation-induced redox modifications was checked by running successive XANES spectra at selected Cr hot spots. No evolution was ever observed showing that the redox states observed can be considered as genuine. (ii) The comparison between maps B and D obtained at incident energies of 6025 and 5997 eV, respectively, reveals a perfect match with an intensity 10 times lower for the incident energy of 5997 eV. This clearly indicates that most chromium is in the trivalent state in agreement with both XPS and solution analyses. Indeed, Cr(VI) compounds present a strong pre-edge peak around 5997 eV, whereas XANES spectra of Cr_2O_3 and other Cr(III) model compounds do not present this characteristic in the pre-edge region (Peterson et al., 1997b). The presence of high proportions of Cr(VI) would then lead to significantly different maps for the two considered incident energies, which is not observed here. (iii) In order to obtain more details about the oxidation state of chromium in various areas of the maps presented in Fig. 7, XANES spectra were recorded (Fig. 8). The features observed indicate the absence of Cr(VI) species and also reveal spectroscopic features significantly different from that of pure Cr_2O_3.

3.5. Iron µXANES experiments

In order to analyze iron species at different points of the maps, XANES spectra were obtained around the iron K-edge. Special attention has been devoted to the pre-edge features, as it has been repeatedly shown (Petit et al., 2001; Wilke et al., 2001; Bonin-Mosbah et al., 2002; Farges et al., 2004) that this region could provide valuable information

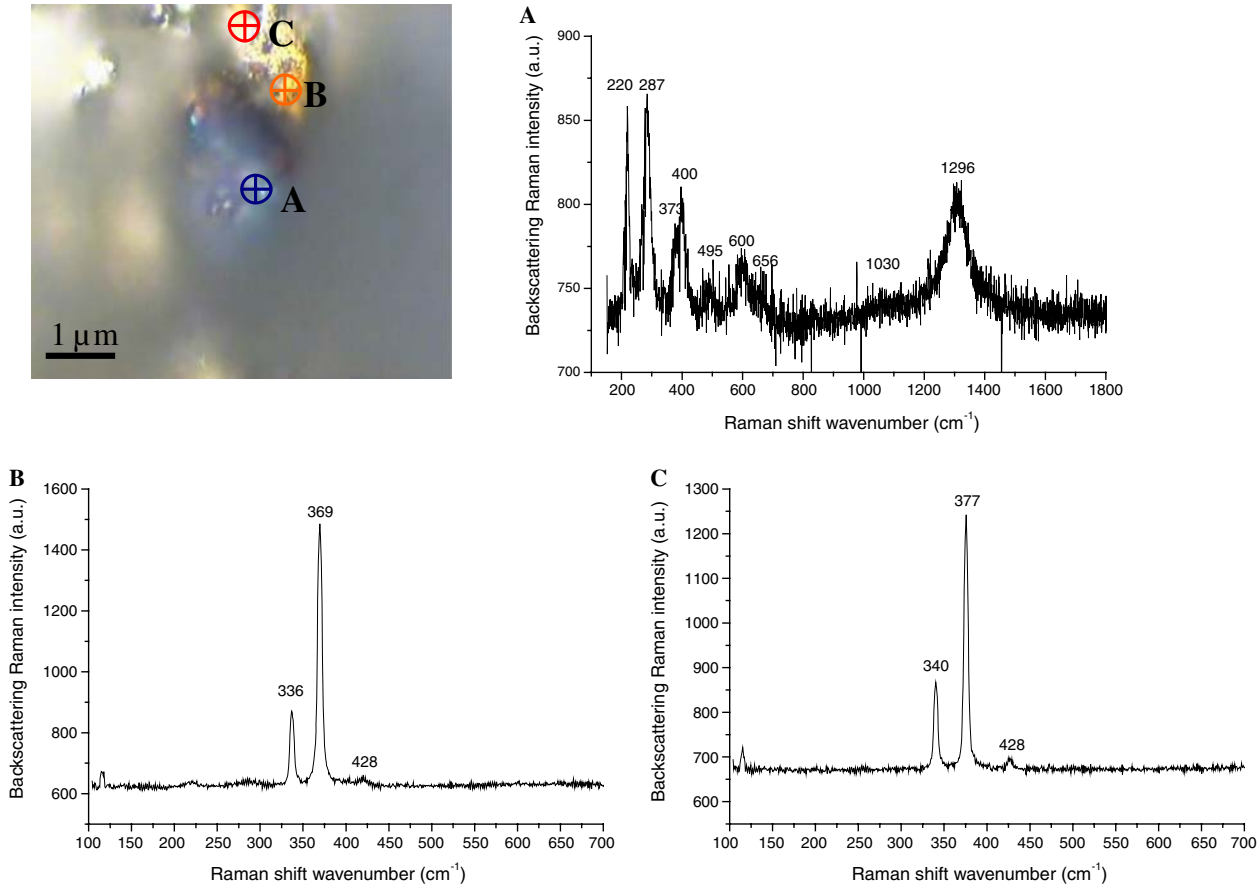

Fig. 6. Optical microscopy image and Raman spectra collected on some representative (A) bluish areas, (B) orange areas and (C) shining particles of pyrite. The experiment was carried out at pH 5 and 4.95×10^{-4} M Cr(VI) initial concentration.

about the degree of oxidation of iron. However, EXAFS spectra at the iron–K edge are not exploitable in the case of the system investigated here as the spectra are dominated by pyrite (data not shown). This confirms Raman results that revealed that surface species had a limited thickness. Fig. 9A displays the pre-edge obtained for washed pyrite, compared to that measured for two specific points of Fig. 7A (1.97×10^{-4} M initial Cr(VI) concentration; pH 5) one rich in chromium (point 1) and the other one poor (point 2) in chromium, whereas Fig. 9B displays the same spectra after subtraction of a baseline determined using a cubic spline. It clearly appears that the two spectra corresponding to washed pyrite and the chromium-poor point are superimposed, whereas a shift towards higher energies is observed for the chromium rich point revealing the presence of ferric ion at this location. Detailed quantitative analysis such as that presented in Farges et al., 2004 , cannot be applied here, as no information is available about the exact thickness of the probed zone. Therefore, it can only be deduced that small amounts of ferric ion are associated with Cr-rich points. Figs. 9C and D show the same analysis in the case of sample with higher Cr content (4.95×10^{-4} M) (Fig. 7B) for a point with a medium chromium content (point 3) and a hot spot in chromium (point 4). In these cases as well, a strong correlation is obtained between chromium amount and relative Fe(III) concentration because the spectrum corresponding to the chromium "hot spot" displays a strong shift at high energy that reveals the presence of increasing amounts of ferric iron.

3.6. Cr K-edge EXAFS

Cr K-edge EXAFS spectra were collected at various points of the different maps (Fig. 7) in order to analyze in more detail the speciation of this element. It must be pointed out that total Cr concentration in the samples is very low (around 50 ppm), so such experiments can only be carried out using microbeam facilities. However, due to the very small size of the spots under analysis and the slight shift of the beam with increasing energy, the EXAFS zone that can be analyzed is only of around 500 eV after the white line. Furthermore, due to the very low concentration in chromium, the raw EXAFS spectra are rather noisy. Fig. 10A presents the raw EXAFS spectrum obtained for a chromium hot spot (point 1 in Fig. 7A) and Fig. 10B displays the corresponding pseudo radial distribution function. Despite the rather low signal/noise ratio, the inverse Fourier transform of the zone between 1.2 and 3.8 Å can be satisfactorily fitted (Fig. 10C) using the parameters described in Table 1. A better fit could certainly be obtained by freeing the number of neighbours. However, in view of the potential complexity of the structure, it appears more

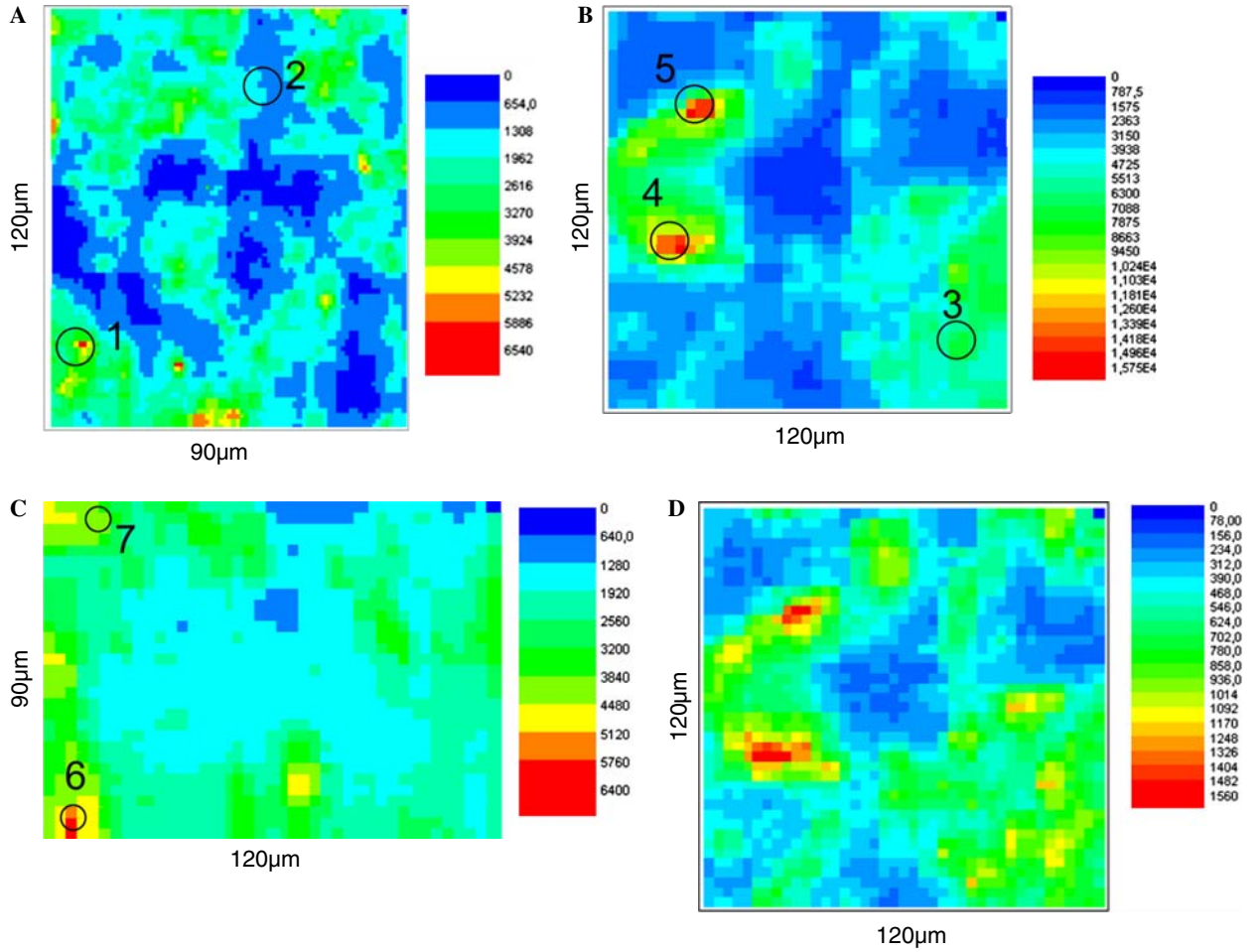

Fig. 7. Spatial chromium distributions obtained by µ-XRF on a pyrite sample reacted at pH 5 with (A) a 1.97×10^{-4} M Cr(VI) solution and (B)–(D) a 4.95×10^{-4} M Cr(VI) solution. Maps (B) and (D) correspond to an analysed area of 120×120 µm with steps displacements of 3 µm and incident X-ray beam energies of 6025 eV and 5997 eV, respectively. Maps (A) and (C) correspond to analysed areas of 90×120 µm with steps displacements of 3 µm and an incident X-ray energy beam of 6025 eV. The various points correspond to areas analysed by Fe XANES and/or Cr EXAFS.

relevant to fix the number of neighbours in the various subshells to compare the results obtained with known crystallographic structures. Furthermore, as far as the nature of backscattering atoms is concerned, it is impossible to distinguish properly between Cr or Fe backscatterers. The result obtained through the fitting procedure (3O at 2.02 Å, 3O at 2.15 Å, 4 metals at 3.06 Å, 3 metals at 3.27 Å and 6 metals at 3.69 Å) is close to an hematite structure (3O at 1.95 Å, 3O at 2.12 Å, 1Fe at 2.90 Å, 3Fe at 2.97 Å, 3Fe at 3.36 Å and 6Fe at 3.75 Å) strongly suggesting that in that case, Cr atoms are involved in a substituted-type hematite structure $Fe_{2-x}Cr_xO_3$, which confirms the results obtained by Raman spectroscopy. Furthermore, it can be inferred that the value of x is in this case rather low as distortion of the structures rapidly occurs for increasing x values (McCarty and Boehme, 1989). In order to show that the fit observed is not simply due to the relatively high number of fitting parameters used in the modeling procedure, Fig. 10D presents a second fit result obtained by fixing the values of the Debye–Waller parameter σ at 0.02 for O–O shells, at 0.02 for Me–Me distances around 2.6 Å, at 0.08 for Cr–Me distances between 3 and 3.3 and at 0.11 for Cr–Me distances higher than 3.4. The fit results thus obtained are slightly less satisfactory (see also the quality factors in Table 1) but reveal very similar structural features. When the amount of adsorbed chromium increases, the situation is a bit different. Indeed, in most cases (Fig. 11 and Table 1), the fits of the filtered EXAFS spectra obtained in various chromium hot spots require the introduction of metallic neighbours around 2.65 Å. Such a distance showing a strongly distorted structure is observed in eskolaite (Cr_2O_3) but not in hematite. Furthermore, in one sample (point 4), a correct fit can be obtained by assuming a single shell of oxygen atoms. In the hematite structure, the two oxygen subshells are well separated (1.95 and 2.12 Å), whereas they are much closer (1.96 and 2.02 Å) in pure Cr_2O_3. It then appears that all the features obtained can be tentatively assigned to a substituted hematite structure $Fe_{2-x}Cr_xO_3$ with relatively high values of x. Such an interpretation validates and refines Raman results in which rel-

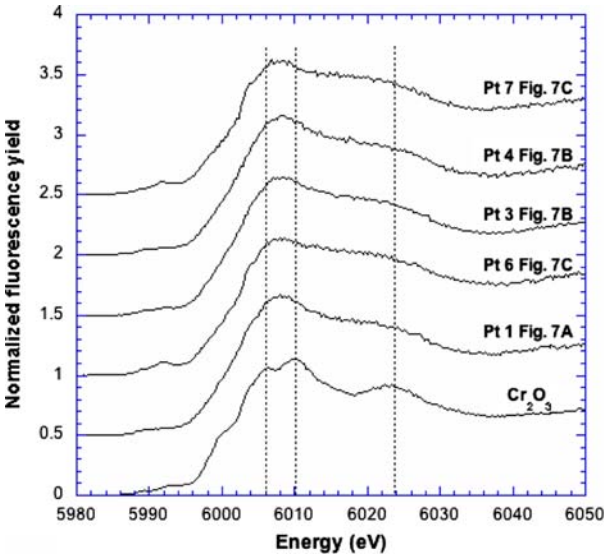

Fig. 8. Chromium K-edge XANES spectra obtained for pure Cr_2O_3 and for various representative points from maps displayed in Fig. 7.

atively high x values could be assumed on the basis of peak width but not ascertained. It must be pointed out, however, that the structure obtained is not pure Cr_2O_3 as revealed by XANES spectra (Fig. 8). The fits of the filtered EXAFS data, though not perfect, also suggest that the amount of Cr substituted in the hematite structure varies for the different hot spots at the pyrite surface. Note that the formation of an overlayer of iron(III)-containing Cr(III) hydroxide at reacted pyrite surface with Cr(VI) solutions has been shown by Doyle et al. (2004) using soft X-ray spectroscopic studies. It must also be noted that one point in the map (Fig. 12 and Table 1) displays a significantly different radial distribution function (RDF) and EXAFS spectrum. The filtered EXAFS data can in this case be very satisfactorily fitted using the distance and number of neighbours in badelleyite (CrOOH) or goethite (FeOOH). The presence of such a compound, that was not evidenced by Raman spectroscopy, suggests either that for elevated initial Cr concentration, some of the chromium can be deposited at the pyrite surface without any direct involvement of iron species, or that mixed iron–chromium oxyhydroxides can also form at the pyrite surface.

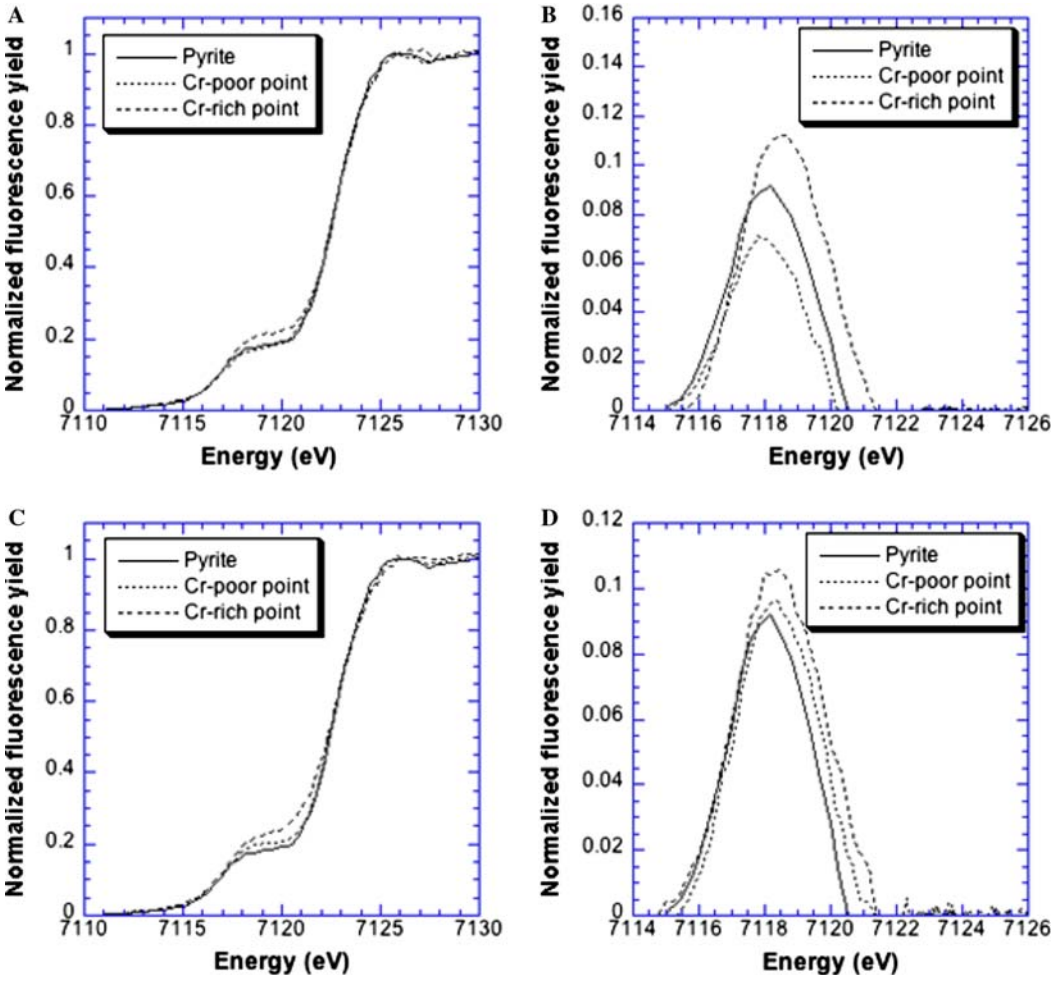

Fig. 9. (A) Normalized XANES spectra in the iron K-edge pre-edge region for pure pyrite and points (1) (Cr-rich) and (2) (Cr-poor) in Fig. 7A; (B) after baseline subtraction; (C) Normalized XANES spectra in the iron K-edge pre-edge region for pure pyrite and points (3) (Cr-medium) and (5) (Cr-rich) in Fig. 7B; (D) after baseline subtraction.

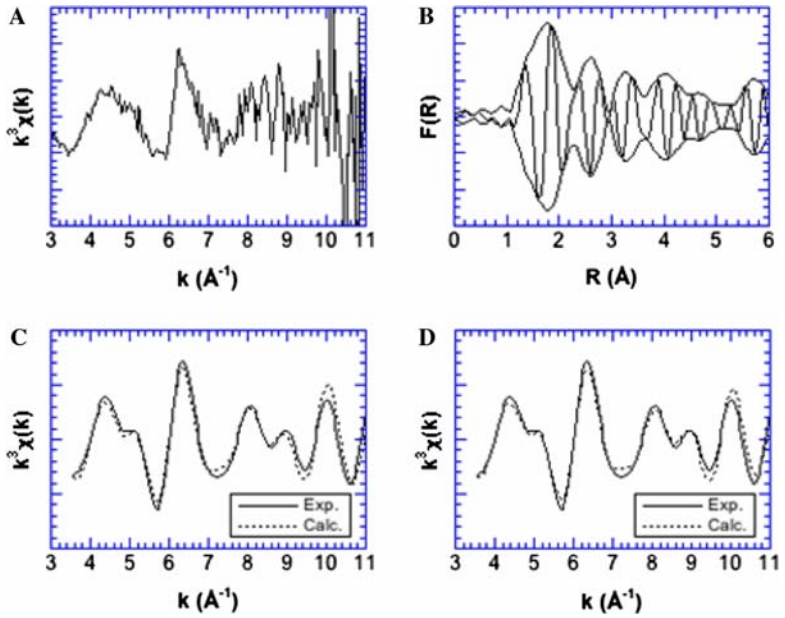

Fig. 10. Raw EXAFS spectrum (A) corresponding pseudo radial distribution function (B), simulations of the inverse Fourier transform between 1.2 and 3.8 $Å^{-1}$ (C and D, see text) obtained at point (1) of map in Fig. 7A.

Table 1
Structural parameters for the first and second coordination sphere of chromium atoms derived from the EXAFS analyses of various points in the maps of Fig. 7

Sample	Shell	Nature	*N*	*R*	σ	*Q*
7A Point 1	1	Oxygen	3 *(3)*	2.02 *(2.00)*	0.02 *(0.02)*	0.057 (*0.078*)
	2	Oxygen	3 (*3*)	2.15 (*2.13*)	0.02 (*0.02*)	
	3	Metal	4 (*4*)	3.06 (*3.04*)	0.06 (*0.08*)	
	4	Metal	3 (*3*)	3.27 (*3.27*)	0.06 (*0.08*)	
	5	Metal	6 (*6*)	3.69 (*3.65*)	0.12 (*0.11*)	
7C Point 6	1	Oxygen	3 (*3*)	1.97 (*1.97*)	0.02 *(0.02)*	0.069 (*0.077*)
	2	Oxygen	3 (*3*)	2.06 (*2.06*)	0.02 (*0.02*)	
	3	Metal	0.5 (*0.5*)	2.63 (*2.61*)	0.05 (*0.02*)	
	4	Metal	4 (*4*)	3.08 (*3.11*)	0.06 (*0.08*)	
	5	Metal	3 (*3*)	3.18 (*3.23*)	0.04 (*0.08*)	
7B Point 3	1	Oxygen	3 (*3*)	1.97 (*1.98*)	0.02 *(0.02)*	0.033 (*0.050*)
	2	Oxygen	3 (*3*)	2.09 (*2.10*)	0.04 (*0.04*)	
	3	Metal	1.2 (*1.0*)	2.58 (*2.57*)	0.02 (*0.02*)	
	4	Metal	4 (*4*)	3.03 (*2.99*)	0.11 (*0.08*)	
	5	Metal	3 (*3*)	3.23 (*3.20*)	0.07 (*0.08*)	
7B Point 4	1	Oxygen	6 (*6*)	2.04 (*2.05*)	0.06 *(0.06)*	0.063 (*0.117*)
	3	Metal	1 (*1.3*)	2.60 (*2.66*)	0.02 (*0.02*)	
	4	Metal	4 (*4*)	3.04 (*3.11*)	0.10 (*0.08*)	
	5	Metal	3 (*3*)	3.22 (*3.24*)	0.05 (*0.08*)	
7C Point 7	1	Oxygen	4 (*4*)	1.94 (*1.95*)	0.05 *(0.04)*	0.012 (*0.043*)
	2	Oxygen	2 (*2*)	2.18 (*2.21*)	0.08 (*0.04*)	
	3	Metal	2 (*2*)	2.95 (*2.94*)	0.02 (*0.02*)	
	4	Metal	2 (2)	3.25 (*3.24*)	0.03 (*0.08*)	
	5	Metal	4 (*4*)	3.42 (*3.37*)	0.12 (*0.11*)	

Values in normal font correspond to the first fit carried out (Figs. 10–12C, see text), values in brackets and italics, to the second fit (Figs. 10–12D, see text).
N, the number of atoms in the first coordination sphere.
R is the distance between the two atoms of each atomic pair.
σ: the Debye–Waller factor (Å).
$Q = \frac{\sum\left[k^3\chi(k)_{\text{calc.}} - k^3\chi(k)_{\text{exp.}}\right]^2}{\sum\left[k^3\chi(k)_{\text{exp.}}\right]^2}$ is the quality factor of the fit.

4. CONCLUSIONS AND PERSPECTIVES

The phenomena occurring upon oxidation of pyrite by Cr(VI) appear to be extremely complex and their study clearly requires the implementation of combined spectroscopic techniques providing complementary information on the speciation of surface compounds. The combination used in this study, particularly the coupling of micro-Raman spectroscopy and micro-X-ray absorption techniques, reveals a systematic association between Fe(III) and Cr(III), that can be found as solid solutions at the pyrite surface. The formation of such chromic–ferric solid solution was previously suggested for Cr(VI) reduction by Fe(II) species (Eary and Rai, 1988; Patterson et al., 1997). However, in most studies, a precise assignment of the formed species was not obtained unequivocally.

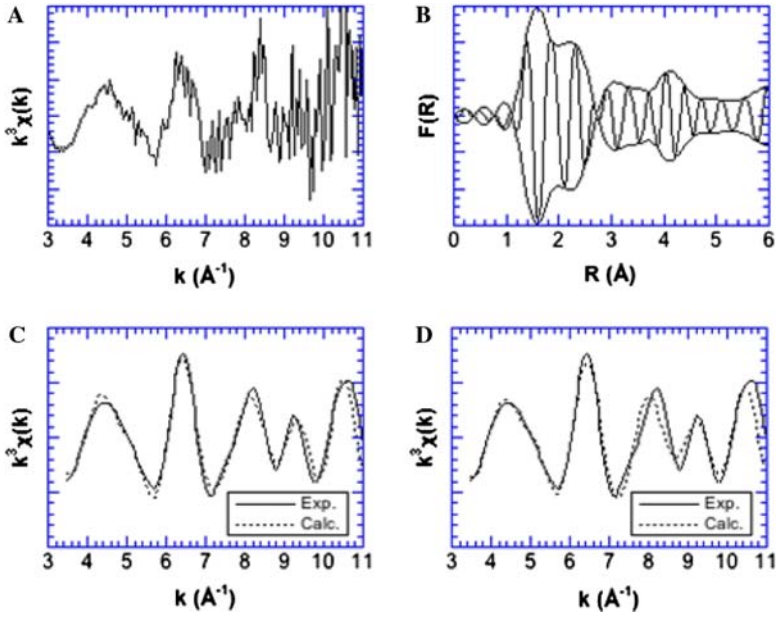

Fig. 11. Raw EXAFS spectrum (A) corresponding pseudo radial distribution function (B), simulations of the inverse Fourier transform between 1.2 and 3.8 $Å^{-1}$ (C and D, see text) obtained at point (3) of map in Fig. 7B.

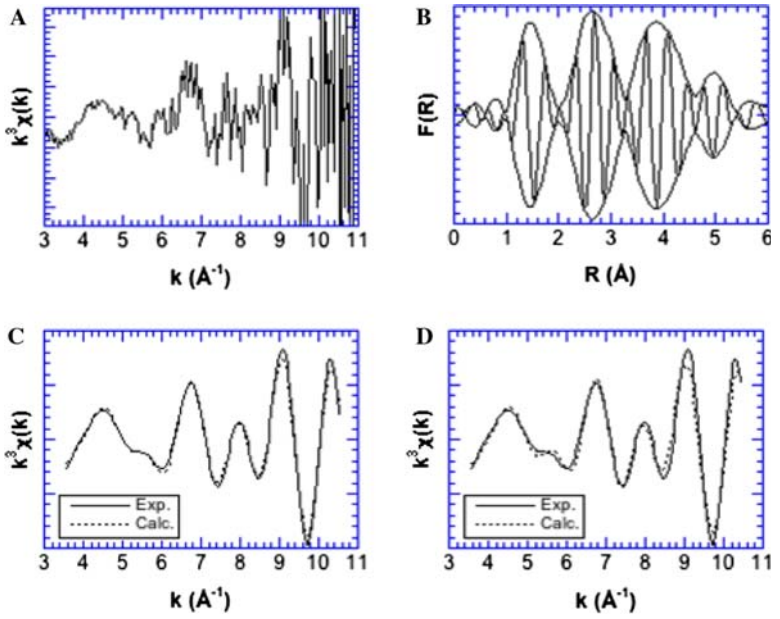

Fig. 12. Raw EXAFS spectrum (A) corresponding pseudo radial distribution function (B), simulations of the inverse Fourier transform between 1.2 and 3.8 $Å^{-1}$ (C and D, see text) obtained at point (7) of map in Fig. 7C.

Doyle et al. (2004) studied the reaction of fractured pyrite surfaces with Cr(VI)-containing aqueous solutions using X-ray photoemission and XANES spectroscopy. Both the starting material and experimental conditions were different from those used in our study. Indeed, we used synthetic pyrite and all our experiments were carried out under an argon atmosphere to limit the presence of oxygen. Furthermore, in addition to photoemission and XANES spectroscopy, we used complementary solution analyses, μ-XRF and micro-Raman spectroscopy to interpret the data. Both studies are consistent with the presence of Cr(III) and iron (III) at the reacted pyrite surfaces. However, Doyle et al. (2004) proposed the formation of an iron(III)-containing Cr(III)-hydroxide whereas we convincingly show the presence at the surface of Cr substituted hematite. In fact, the most frequently encountered mixed Cr–Fe species is $Fe_{2-x}Cr_xO_3$. In order to unravel in more detail the reaction mechanisms, the present study should be complemented by sulphur species analyses, which will be presented in our next paper. Such studies are of particular interest to determine the origin of the areas displaying a characteristic drifts in the Raman bands of pyrite of about -3 and $-6\ cm^{-1}$. These drifts that could be assigned to a local increase in the electronic density, are probably related to anodic cathodic reactions as previously discussed by Rimstidt and Vaughan (2003). Furthermore, in view of the complexity of the various reactions occurring simultaneously, it appears that a much more detailed understanding of the mechanisms occurring at the pyrite surface could be obtained by working on model pyrite surfaces in which the nature of the crystalline faces can be controlled, in order to link the heterogeneity observed on powdered systems with structural data. Finally, in a longer term perspective, it would be extremely relevant to compare the mechanisms occurring upon chemical oxidation with those involved in bacteria-mediated oxidation as various studies have already revealed that the corrosion figures obtained with bacteria are significantly different from those obtained by chemical attacks (Toniazzo et al., 1996).

ACKNOWLEDGMENTS

X-ray absorption spectroscopy was performed at the Swiss Light Source, Paul Scherrer Institut, Villigen, Switzerland. We are grateful to the machine and beamline groups whose outstanding efforts have made these experiments possible. We particularly thank A.-M. Flank for fruitful discussions. This research project has been supported by the European Commission under the 6th Framework Programme through the Key Action: Strengthening the European Research Area, Research Infrastructures. Contract no.: RII3-CT-2004-506008. The authors acknowledge J. Lambert from the Laboratoire de Chimie Physique et Microbiologie pour l'Environnement for the XPS analyses.

REFERENCES

Allen G. C., Curtis M. T., Hooper A. J., and Tucker P. M. (1974) X-ray photoelectron spectroscopy of iron-oxygen systems. *J. Chem. Soc., Dalton Trans.: Inorg. Chem.* **14**, 1525–1530.

Baes C. F., and Mesmer R. E. (1976) *The Hydrolysis of Cations*. Wiley-Interscience Publication, New-York, p. 489.

Barbillat J., Dhamelincourt P., Delhaye M., and Da Silva E. (1994) Raman confocal microprobing, imaging and fiber optic remote sensing: a further step in molecular analysis. *J. Raman Spectrosc.* **25**, 3–8.

Bonin-Mosbah M., Metrich N., Susini J., Salome M., Massare D., and Menez B. (2002) Micro X-ray absorption near edge structure at the sulphur and iron K-edges in natural silicate glasses. *Spectrochim. Acta, B-Atomic Spectrosc.* **57**, 711–725.

Brett J. B., and Banfield J. F. (2003) Microbial communities in acid mine drainage. *FEMS Microbiol. Ecol.* **44**, 139–152.

Buerge I. J., and Hug S. J. (1997) Kinetics and pH dependence of chromium(VI) reduction by iron(II). *Environ. Sci. Technol.* **31**, 1426–1432.

Davis A., Fennemore G. G., Peck C., Walker C. R., McIlwraith J., and Thomas S. (2003) Degradation of carbon tetrachloride in a reducing groundwater environment: implications for natural attenuation. *Appl. Geochem.* **18**, 503–525.

De Faria D. L. A., Silva S. V., and De Oliviera M. T. (1997) Raman microspectroscopy of some iron oxides and oxyhydroxides. *J. Raman Spectrosc.* **28**, 873–878.

Demoisson F., Mullet M., and Humbert B. (2005) Pyrite oxidation by hexavalent chromium: Investigation of the chemical processes by monitoring of aqueous metal species. *Environ. Sci. Technol.* **39**, 8747–8751.

Doyle C. S., Kendelewicz T., Bostick B. C., and Brown G. E. (2004) Soft X-ray spectroscopic studies of the reaction of fractured pyrite surfaces with Cr(VI)-containing aqueous solutions. *Geochim. Cosmochim. Acta* **68**, 4287–4299.

Eary L. E., and Rai D. (1988) Chromate removal from aqueous wastes by reduction with ferrous ion. *Environ. Sci. Technol.* **22**, 972–977.

Eary L. E., and Rai D. (1989) Kinetics of chromate reduction by ferrous ions derived from hematite and biotite at 25 °C. *Am. J. Sci.* **289**, 180–213.

Eggleston C. M., Ehrhardt J. J., and Stumm W. (1996) Surface structural controls on pyrite oxidation kinetics: an XPS-UPS, STM and modelling study. *Am. Mineral.* **81**, 1036–1056.

Farges F., Lefrère Y., Rossano S., Berthereau A., Calas G., and Brown, Jr., G. E. (2004) The effect of redox state on the local structural environment of iron in silicate glasses: a combined XAFS spectroscopy, molecular dynamics, and bond valence study. *J. Non-Cryst. Solids* **344**, 176–188.

Fendorf S. E., and Li G. (1996) Kinetics of chromate reduction by ferrous iron. *Environ. Sci. Technol.* **30**, 1614–1617.

Flank A.-M., Cauchon G., Lagarde P., Bac S., Janousch M., Wetter R., Dubuisson J.-M., Idir M., Langlois F., Moreno T., and Vantelon D. (2006) LUCIA, a microfocus soft XAS beamline. *Nucl. Instr. Meth.* **246**, 269–274.

Francis A. J., Dodge C. J., Rose A. W., and Ramirez A. J. (1989) Aerobic and anaerobic microbial dissolution of toxic metals from coal wastes: mechanism of action. *Environ. Sci. Technol.* **23**, 435–441.

Hansford G. S., and Vargas T. (2001) Chemical and electrochemical basis of bioleaching processes. *Hydrometallurgy* **59**, 135–145.

Hart T. R., Adams S. B., and Temkin H. (1975) Raman scattering from phonons and magnons in $\alpha-Fe_2O_3$. In *Proceedings of the Third International Conference on Light Scattering in Solids*, (eds. M. Balkanski, R. C. C. Leite and S. P. S. Porto). Wiley, pp. 259–263.

Ikemoto I., Ishii K., Kinoshita S., Kuroda H., Alario Franco M. A., and Thomas J. M. (1976) X-ray photoelectron spectroscopic studies of CrO_2 and some related chromium compounds. *J. Solid State Chem.* **17**, 425–430.

Kendelewicz T., Liu P., Doyle C. S., and Brown G. E. (2000) Spectroscopic study of the reaction of aqueous Cr(VI) with Fe_3O_4 (1 1 1) surfaces. *Surf. Sci.* **469**, 144–163.

Kim J. G., Jung P.-K., Moon H.-S., and Chon C.-M. (2002) Reduction of hexavalent chromium by pyrite-rich andesite in different anionic solutions. *Environ. Geol.* **42**, 642–648.

Kirkpatrick P., and Baez A. V. (1948) Formation of optical images by X-rays. *J. Opt. Soc. Am.* **38**, 766–774.

Lowson R. T. (1982) Aqueous oxidation of pyrite by molecular oxygen. *Chem. Rev.* **82**, 461–497.

Loyaux-Lawniczak S., Refait P., Ehrhardt J.-J., Lecomte P., and Genin J.-M. (2000) Trapping of Cr by formation of ferrihydrite during the reduction of chromate ions by Fe(II)–Fe(III) hydroxysalt green rusts. *Environ. Sci. Technol.* **34**, 438–443.

Martin T. P., Merlin R., Huffman D. R., and Cardona M. (1977) Resonant two magnon Raman scattering in α-Fe_2O_3. *Solid State Commun.* **22**, 565–567.

Massey M. J., Baier U., Merlin R., and Weber W. H. (1990) Effects of pressure and isotopic substitution on the Raman spectrum of α-Fe_2O_3: identification of two magnon scattering. *Phys. Rev. B* **41**, 7822–7827.

McCarty K. F., and Boehme D. R. (1989) A Raman study of the systems $Fe_{3-x}Cr_xO_4$ and $Fe_{2-x}Cr_xO_3$. *J. Solid State Chem.* **79**, 19–27.

McIntyre N. S., and Zetaruk D. G. (1977) X-ray photoelectron spectroscopic studies of iron oxide. *Anal. Chem.* **49**, 1521–1529.

McKibben M. A., and Barnes H. L. (1986) Oxidation of pyrite in low temperature acidic solutions: rate laws and surface textures. *Geochim. Cosmochim. Acta* **50**, 1509–1520.

Michalowicz A. (1990). Méthodes et programmes d'analyse des spectres d'absorption des rayons X (EXAFS). Applications à l'étude de l'ordre local et du désordre cristallin dans les matériaux inorganiques. PhD Thesis. Université Paris-Val de Marne.

Moses Carl O., Nordstrom D. K., Herman J. S., and Mills A. L. (1987) Aqueous pyrite oxidation by dissolved oxygen and by ferric iron. *Geochim. Cosmochim. Acta* **51**, 1561–1571.

Mullet M., Boursiquot S., and Ehrhardt J.-J. (2004) Removal of hexavalent chromium from solutions by mackinawite, tetragonal FeS. *Colloid. Surf. A* **244**, 77–85.

Myers C. R., Myers J. M., Carstens B. P., and Antholine W. E. (2000) Reduction of chromium(VI) to chromium(V) by human microsomal enzymes: effects of iron and quinones. *Tox. Subst. Mech.* **19**, 25–51.

Nesbitt H. W., Bancroft G. M., Pratt A. R., and Scaini M. J. (1998) Sulfur and iron surface states on fractured pyrite surfaces. *Am. Mineral* **83**, 1067–1076.

Norseth T. (1981) The carcinogenicity of chromium. *Environ. Health Persp.* **40**, 121–130.

Patterson R. R., Fendorf S., and Fendorf M. (1997) Reduction of hexavalent chromium by amorphous iron sulfide. *Environ. Sci. Technol.* **31**, 2039–2044.

Peterson M. L., Brown, Jr., G. E., Parks G. A., and Stein C. L. (1997a) Differential redox and sorption of Cr(III/VI) on natural silicate and oxide minerals: EXAFS and XANES results. *Geochim. Cosmochim. Acta* **61**, 3399–3412.

Peterson M. L., White A. F., Brown, Jr., G. E., and Parks G. A. (1997b) Surface passivation of magnetite by reaction with aqueous Cr(VI): XAFS and TEM results. *Environ. Sci. Technol.* **31**, 1573–1576.

Petit P. E., Farges F., Wilke M., and Solé V. A. (2001) Determination of the iron oxidation state in Earth materials using XANES pre-edge information. *J. Synchrotron. Radiat.* **8**, 952–954.

Pettine M., D'Ottone L., Campanella L., Millero F. J., and Passino R. (1998) The reduction of chromium (VI) by iron (II) in aqueous solutions. *Geochim. Cosmochim. Acta* **62**, 1509–1519.

Rimstidt J. D., and Vaughan D. J. (2003) Pyrite oxidation: a state-of-the-art-assessment of the reaction mechanism. *Geochim. Cosmochim. Acta* **67**, 873–880.

Rodriguez Y., Ballester A., Blazquez F., Gonzalez F., and Munoz J. A. (2003) New information on the pyrite bioleaching mechanism at low and high temperature. *Hydrometallurgy* **71**, 37–46.

Schaufuß A. G., Nesbitt H. W., Kartio I., Laajalehto K., Bancroft G. M., and Szargan R. (1998) Incipient oxidation of fractured pyrite surfaces in air. *J. Elect. Spectrosc. Relat. Phenom.* **96**, 69–82.

Schlautman M. A., and Han I. (2001) Effects of pH and dissolved oxygen on the reduction of hexavalent chromium by dissolved ferrous iron in poorly buffered aqueous systems. *Water Res.* **35**, 1534–1546.

Shim S. H., and Duffy T. S. (2001) Raman spectroscopy of Fe_2O_3 to 62 GPa. *Am. Mineral.* **87**, 318–326.

Shirley D. A. (1972) High-resolution X-ray photoemission spectrum of the valence bands of gold. *Phys. Rev. B* **5**, 4709.

Sourisseau C., Cavagnat R., and Fouassier M. (1991) The vibrational properties and valence force fields of iron disulfide, ruthenium disulfides pyrites and FeS_2 marcasite. *J. Phys. Chem. Solids* **52**, 537–544.

Teo B. K. (1986) *EXAFS: Basic Principles and Data Analysis*. Springer, Berlin Heidelberg, New-York.

Tokunaga T. K., Wan J. M., Firestone M. K., Hazen T. C., Olson K. R., Herman D. J., Sutton S. R., and Lanzirotti A. (2003) In situ reduction of chromium(VI) in heavily contaminated soils through organic carbon amendment. *J. Environ. Qual.* **32**(5), 1641–1649.

Toniazzo, V., Mustin, C., Vayer-Besancon, M., Erre, R., Berthelin, J., 1996. An XPS and AFM coupled study of air and bio-oxidized pyrite surfaces. Effect of Mineral-Organic-Microorganism Interactions on Soil and Freshwater Environments. In: *Proceedings of an International Symposium on the Effect of Mineral-Organic-Microorganism Interactions on Soil and Freshwater Environments*, second ed. Nancy, France.

Vaughan D. J., and Lennie A. R. (1991) The iron sulfide minerals: their chemistry and role in nature. *Sci. Prog.* **75**, 371–388.

Vogt H., Chattopadhyay T., and Stolz H. J. (1983) Complete first-order Raman spectra of the pyrite structure compounds FeS_2, MnS_2 and SiP_2. *J. Phys. Chem. Solids* **44**, 869–873.

Wilke M., Farges F., Petit P. E., Brown G. E., and Martin F. (2001) Oxidation state and coordination of Fe in minerals: an FeK-Xanes spectroscopic study. *Am. Mineral* **86**, 714–730.

Williams AG., and Scherer M. M. (2001) Kinetics of Cr(VI) reduction by carbonate green rust. *Environ. Sci. Technol.* **35**, 3488–3494.

Zabinsky S. I., Rehr J. J., Ankudinov A., Albers R. C., and Eller M. J. (1995) Multiple scattering calculations of X-ray absorption spectra. *Phys. Rev. B* **52**, 2995–3009.

Zouboulis A. I., Kydros K. A., and Matis K. A. (1993) Removal of toxic metal ions from solutions using industrial solid by products. *Water Sci. Technol.* **27**, 83–93.

Zouboulis A. I., Kydros K. A., and Matis K. A. (1995) Removal of hexavalent chromium anions from solutions by pyrite fines. *Water Res.* **29**, 1755–1760.

Associate editor: Carrick M. Eggleston